CHEMISTRY OF MATERIALS

pubs.acs.org/cm

Perspective

Development of a Geometric Descriptor for the Strategic Synthesis of Remeika Phases

Alexis Dominguez Montero, Gregory T. McCandless, Olatunde Oladehin, Ryan E. Baumbach, and Julia Y. Chan*

Cite This: *Chem. Mater.* 2023, 35, 2238−2247

Read Online

ACCESS | Metrics & More | Article Recommendations | Supporting Information

ABSTRACT: Remeika phases, also described as pseudoperovskites, are cage-like structures with emergent properties. In this Perspective, we first cover heuristic methods used to overcome the challenges to rationalize the stability of extended solids. We highlight the important role Goldschmidt's tolerance factor has played in enhancing research related to perovskites and their derivatives. We discuss the development of a tolerance factor for predicting the stability of intermetallic pseudoperovskites, the Remeika phases, and rationalize oxidation states in correlation with valence fluctuation. To evaluate the feasibility of the Remeika phase tolerance factor, we synthesized the new predicted compound $Yb_5Ru_6Sn_{18}$ with a magnetic moment (μ_{eff}) of 3.2 μ_B/Yb. We then highlight the importance of determining the factors dictating the stability of the Remeika intermetallics.

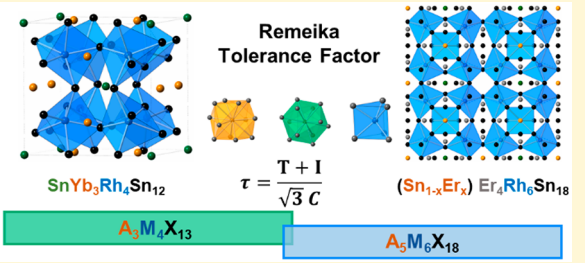

I. INTRODUCTION

Throughout history, discovering new materials has been a forerunner of technological advancement. There are examples from the early stages of civilization, such as the discovery of bronze, to modern times, with synthesized silicon semiconductors and their impact in modern computation and quantum materials. Solid state synthesis remains a challenge in extended solids where phase formation, the temperature profile, and reaction ratios can lead to unpredictability.[1] Nevertheless, solid state chemists have implemented chemical heuristics, such as periodic trends, the Zintl−Klemm concept,[2] Pauling's rules,[3,4] Wade−Mingo's rules,[5,6] the valence electron concentration,[7,8] and geometrical constraints, to predict the results. A straightforward path for finding isostructural compounds could be keeping constant all of the elements of the structure of interest, except for one, which would be replaced by a chemically similar element. However, this does not allow extrapolation to other combinations of elements, hindering exploratory growth. Employing chemical heuristics accelerates the study of specific crystal structures with little to no computation power. As mentioned by Canfield, one can explore the known unknown structures "start[ing] by the campfire and walk[ing] out, exploring the edges or peripheries" and what better than bringing a flashlight to explore further.[9]

Intermetallics have been described by their bonding and electronic structure, for instance, Hume−Rothery phases, polar intermetallics, and Zintl phases.[10] Hume−Rothery phases form between metals with similar electronegativity and size, where optimum packing with delocalized bonding is preferred. On the contrary, Zintl phases form between elements with significant differences between their electronegativities, where a complete electron transfer occurs between a covalently bonded anionic framework and a cation. However, between both classifications are the polar intermetallic compounds, which present both covalent and ionic bonding, where only a partial charge transfer occurs between the cation and anionic framework, thus showing deviations from the ideal valence electron counting expected for Zintl phases.[10] In general, the interplay among valence electron counting, Madelung energies, and optimum packing determines the structural stability of polar intermetallics.[11] Valence electron counting rules govern the stability of Zintl phases, while the Madelung energy and optimum packing are key factors for polar intermetallics. The valence electron concentration, which is the ratio between the number of valence electrons and atoms, is used to classify intermetallics (Figure 1).[8,10]

II. ELECTRON COUNTING AND GEOMETRICAL DESCRIPTORS

Valence electron counting can be used for intermetallic families to predict the stability of compounds and their properties. For instance, Corbett et al. highlighted the relationship between valence electron counting (VEC) and

Received: December 15, 2022
Revised: February 22, 2023
Published: March 9, 2023

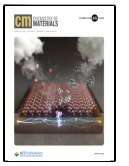

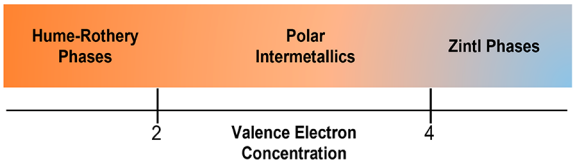

Figure 1. Approximate classification of Hume−Rothery phases, polar intermetallics, and Zintl phases based on valence electron concentration.[8,10]

the phase stability of three distinct ordered variants of the $BaAl_4$ structure type ($BaNiSn_3$, $ThCr_2Si_2$, and $CaBe_2Ge_2$ structure types) in the Ba−Au−Sn system.[7] Similarly, VEC was probed in metal disilicides where the use of the 14-electron rule enabled the prediction of the ordered semiconductor ReGaSi.[12] Analogous to the 14-electron rule, the Zintl counting formalism has been used to extend the filled skutterudites to group 9 transition metal compounds, where a valence electron count of 96 would lead to stable semiconducting materials.[13] The 96-electron count was later encompassed within the $18 - n + m$ rule for multiple binaries in addition to the skutterudites. The $18 - n + m$ rule consists of an electron counting rule for transition metal−main group binary intermetallics, where n is the number of electron pairs shared between transition metals or lanthanides and m the average number of electron pairs of noninteracting p-block elements per transition metal/lanthanide.[14] In the case of the $CoAs_3$ structure type, Fredrickson et al. determined 24 electrons are necessary to fulfill the $18 - n + m$ rule.[14] The agreement between the Zintl counting formalism for the filled skutterudites and the $18 - n + m$ rule for the binary skutterudite can be rationalized by normalizing the necessary valence electrons per transition metal.

Geometrical descriptors have been used throughout the years in multiple crystal structures as a fast screening of phase stability due to facile calculation requiring only the radius and a predefined mathematical equation. The geometrical descriptors relate the chemical composition of the structures with the structural motifs by using the radius and crystallographic sites of the constituents. Geometrical constraints, such as tolerance factors, thus far, have been applied to predict the structural stabilities of ionic compounds. For example, perovskites,[15] pyrochlores,[16] and normal spinels[17] are families of compounds that have benefitted from the use of tolerance factors. For instance, the development of a geometrical constraint, such as Goldschmidt's tolerance factor, has predicted structural distortion in the perovskite structure from the ionic radii of the constituent elements.[15] Goldschmidt's tolerance factor serves as a first predictive screen when searching for new perovskite structures. Phases adopting an ideal perovskite structure have a Goldschmidt's tolerance factor value of 1, while those with structural distortion have values of <1. The perovskite structure consists of corner-sharing octahedra $[BX_6]$, where the cuboctahedral void formed is filled by the A cation. The structure type is robust and has been extensively studied because of its diverse functionalities and applications in energy materials,[18] such as superconductivity, electrical,[19] magnetic, and optoelectronic applications,[20] and even more recently, the discovery of nickelate superconductivity.[21]

The ionic character of perovskites enables the formation of related structures due to charge balancing; this constraint has been utilized to synthesize structures, such as the double perovskites $A_2B'B''X_6$ or oxygen deficient perovskites that have shown promising magnetic and electrical properties.[22] For instance, Sr_2FeMoO_6[22] yields colossal magnetoresistance while magnetism and superconductivity coexist in $Sr_2YRu_{1-x}Cu_xO_6$.[23] Other perovskite derivatives are the antiperovskites with the general formula A_3XY that consist of the same structural motifs as the perovskites, but with inverted cation−anion sites. The high ionic conductivity of $Li_3OCl_{0.5}Br_{0.5}$[24] has suggested antiperovskites are promising materials for solid state batteries.[25,26] We can observe the utility of Goldschmidt's tolerance factor due to its ability not only to predict perovskites and their derivatives, such as the double perovskites, antiperovskites, layered perovskites, and hybrid analogues, but also to relate physical properties with such values.[18,26−29]

III. REMEIKA PHASES: A PLATFORM FOR INTERMETALLIC PSEUDOPEROVSKITES

In this Perspective, our goal is to exemplify the utility of heuristic methods such as a tolerance factor to predict the stability of the intermetallic pseudoperovskites, the Remeika phases. Due to the discovery of heavy fermion electron systems in $Ce_3Co_4Sn_{13}$,[30] superconductivity in $Lu_3M_4Ge_{13-x}$ (M = Co, Rh, and Os) and $Y_3M_4Ge_{13-x}$ (M = Ir, Rh, and Os),[31] and intermediate valence electron systems such as $Yb_3(Rh_{1-x}M_x)_4Ge_{13}$ (M = Co and Ir) through quantum phase transitions,[32] our group found it imperative to determine plausible Remeika phases. We present a new geometrical descriptor for the Remeika phases, demonstrate its feasibility by synthesizing the predicted compound $Yb_5Ru_6Sn_{18}$, and provide insight into the structure−property relationships. The Remeika phase provides a platform for studying the interplay among the electronic structure, geometrical constraints, and their effects on physical properties.

III.A. Structure Types and Geometric Descriptor. Inspired by the magnetic and/or superconducting ternary A−Rh−Sn (A = alkali metals, Sc, Y, lanthanides, and actinides) system presented by Remeika et al.,[33] Espinosa et al. identified seven distinct structures as part of the Remeika phases grown by Sn flux.[34] The presented structures were classified on the basis of the crystal system adopted; such phases were primitive cubic (phase 1), body-centered tetragonal (phase 2), face-centered cubic (phase 3), slightly distorted phase one (phase 4), body-centered cubic (phase 5/Ir_3Ge_7 structure type), an unidentified phase (phase 6), and a distorted phase five (phase 7). For the scope of this Perspective and due to their structural relationship, we will focus on phases 1−3 as shown in Table 1.

Table 1. Summary of Three Selected Remeika Phases

phase	crystal system	structure type	refs
1	primitive cubic	$Yb_3Rh_4Sn_{13}$	35, 36
2	body-centered tetragonal	$(Sn_{1-x}Er_x)Er_4Rh_6Sn_{18}$	37
3	face-centered cubic	$(Sn_{1-x}Tb_x)Tb_4Rh_6Sn_{18}$	36

III.A.1. $Yb_3Rh_4Sn_{13}$ Structure Type. Compounds with the $Yb_3Rh_4Sn_{13}$ structure type (Figure 2) are intermetallics with a stoichiometry of $A_3M_4X_{13}$ (A = alkali metals, Sc, Y, lanthanides, and actinides; M = transition metals from groups 8−10; and X = Si, Ge, In, Sn, and Pb) that were first discovered in 1980 by Remeika and co-workers and denoted as phase 1, as shown in Table 1.[33]

The $Yb_3Rh_4Sn_{13}$ structure type (space group $Pm\bar{3}n$) consists of a three-dimensional (3D) array of corner-sharing trigonal

https://doi.org/10.1021/acs.chemmater.2c03711
Chem. Mater. 2023, 35, 2238−2247

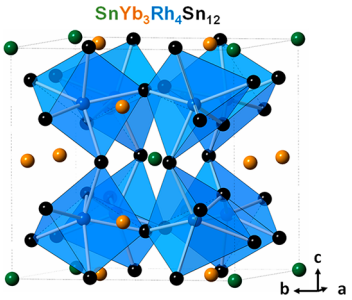

Figure 2. Crystal structure of $Yb_3Rh_4Sn_{13}$ depicting the corner-sharing trigonal prisms [$RhSn_6$].

prisms [MX_6] where the formed cuboctahedral and icosahedral cavities are filled by the electropositive element [AX_{12}] and p-block element [X_1X_{12}], respectively. It is important to note that there are two crystallographically unique Sn sites; one Sn occupies the icosahedral cage (Wyckoff site 2*a*), and the remaining 12 Sn atoms form the framework (Wyckoff site 24*k*). The $Yb_3Rh_4Sn_{13}$ structure type can be considered an intermetallic pseudoperovskite structure and was first described as a cage-like structure where positively charged metals fill a covalently bonded framework formed by the main group element.[35] To exemplify the local environments of the $Yb_3Rh_4Sn_{13}$ structure type and their relationship with the perovskite structure, the first Remeika compound, $Yb_3Rh_4Sn_{13}$, is depicted in Figure 3. By considering the formula, we obtain $SnYb_3Rh_4Sn_{12}$, which is a multiple (4×) of the perovskite general formula ABX_3.

Structural lower-symmetry models, hettotypes, have been reported, and their relationship to the $Yb_3Rh_4Sn_{13}$ structure type, aristotype, can be explained on the basis of group−subgroup schemes.[38,39] A summary of the lower-symmetry derivatives of the $Yb_3Rh_4Sn_{13}$ structure type was provided by Oswald et al.[38] The $Yb_3Rh_4Sn_{13}$ structure type and its hettotypes are of interest due to the wide spectrum of physical properties, such as the coexistence of superconductivity and charge density waves in a 3D structure,[40−43] the presence of a quantum critical point through pressure and/or chemical substitution,[44,45] and Weyl−Kondo semimetal in a chiral phase,[46] to mention a few.

III.A.2. $(Sn_{1-x}Er_x)Er_4Rh_6Sn_{18}$ and $(Sn_{1-x}Tb_x)Tb_4Rh_6Sn_{18}$. These structure types are polar intermetallics with a stoichiometry of $A_5M_6X_{18}$ (A = Sc, Y, Zr, and lanthanides; M = transition metals from groups 8−10; and X = Ge, In, Sn, Pb, and Bi). Remeika et al. classified such structures as body-centered tetragonal (phase 2) and face-centered cubic (phase 3), respectively.[33] Similar to the $Yb_3Rh_4Sn_{13}$ structure type, the $(Sn_{1-x}Er_x)Er_4Rh_6Sn_{18}$ structure type consists of a 3D array of corner-sharing trigonal prisms [BX_6] where the A element fills a cuboctahedral void. However, the difference shown in Figure 4 between $Yb_3Rh_4Sn_{13}$ and $(Sn_{1-x}Tb_x)Tb_4Rh_6Sn_{18}$ structure types resides in the prism arrangement, thus causing two distinct crystallographic sites for the A element. A detailed comparison between the $Yb_3Rh_4Sn_{13}$ and $(Sn_{1-x}Tb_x)$-$Tb_4Rh_6Sn_{18}$ structure types is provided by Hodeau et al.[37] The $(Sn_{1-x}Er_x)Er_4Rh_6Sn_{18}$ structure type and its hettotype analogues have been of interest due to reports of tunability between reentrant superconductivity and magnetic ordering in $(Sn_{1-x}Er_x)Er_4M_6Sn_{18}$ (M = Rh and Os),[47,48] unconventional superconductivity in $A_5Rh_6Sn_{18}$ (A = Lu, Y, and Sc),[49−51] noncollinear spin structure,[52] and disorder-enhanced non-homogeneous superconductivity in the $Y_{5-\delta}(Rh_{5.5}M_{0.5})Sn_{18}$ compounds.[53]

III.B. Development of a Remeika Tolerance Factor. We sought to investigate the chemical and geometrical constraints determining the phase stability of Remeika phases 1−3 and their lower-symmetry variants. As labeled in Figure 5, we will define the heights of the trigonal prism as *T*, the distance between opposite equilateral triangular faces in the icosahedra as *I*, and that of the cuboctahedron as *C*. To develop the tolerance factor for the $Yb_3Rh_4Sn_{13}$ structure type, we first related the structural motifs present in the structure type to the unit cell. For instance, in Figure 5a we can observe the equivalence between the body diagonal of the cubic unit cell (*D*) and the sum between the heights of two trigonal prisms (2*T*) and two icosahedra (2*I*), as shown in eq 1. The diagonal of a cube (*D*) and the length of the same (*a*) can be related through eq 2. By substituting eq 2 into eq 1 and solving for the length of the unit cell (*a*), we obtain eq 3. Next, we can relate the width of two cuboctahedra (2*C*) and the length of the unit cell (*a*) as observed in Figure 5b, obtaining eq 4.

$$2T + 2I = D \tag{1}$$

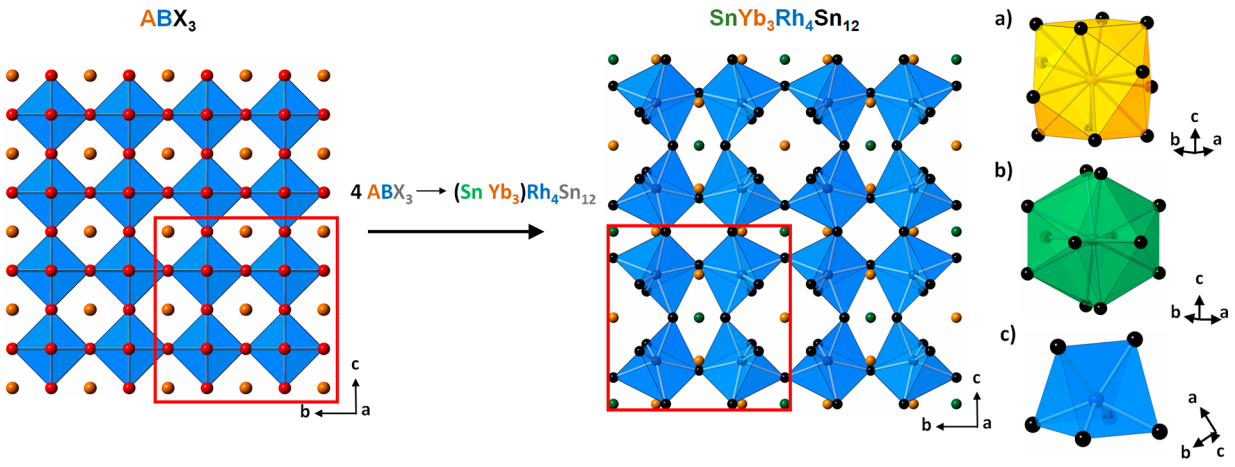

Figure 3. Crystal structures of perovskites and $Yb_3Rh_4Sn_{13}$, showing their structural similarities. Local environments of (a) Yb, (b) Sn, and (c) Rh in the $Yb_3Rh_4Sn_{13}$ structure type.

https://doi.org/10.1021/acs.chemmater.2c03711
Chem. Mater. 2023, 35, 2238−2247

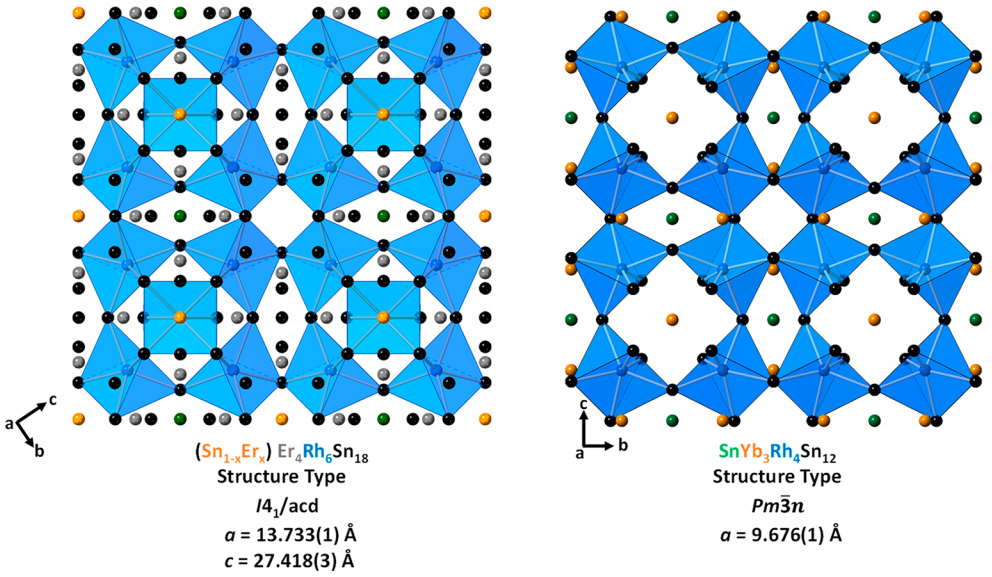

Figure 4. Structural comparison between the $(Sn_{1-x}Er_x)Er_4Rh_6Sn_{18}$ (left) and $Yb_3Rh_4Sn_{13}$ (right) structure types. The $(Sn_{1-x}Er_x)Er_4Rh_6Sn_{18}$ unit cell is partially shown for direct comparison with the cubic $Yb_3Rh_4Sn_{13}$ structure type.

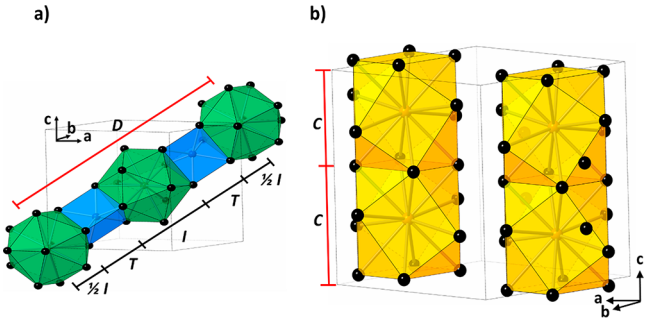

Figure 5. (a) Body diagonal of the cubic unit cell and its relationship to the icosahedral and trigonal prism structural motifs. (b) Length of the cubic unit cell and its relationship to the cuboctahedral structural motif.

$$D = a\sqrt{3} \tag{2}$$

$$\frac{2T + 2I}{\sqrt{3}} = a \tag{3}$$

$$2C = a \tag{4}$$

$$T = 2\sqrt{(r_M + r_X)^2 - \frac{4r_X^2}{3}} \tag{5}$$

$$I = 2\sqrt{(r_X + r_Y)^2 - \frac{4r_X^2}{3}} \tag{6}$$

$$C = 2\sqrt{(r_A + r_X)^2 - (r_M + r_X)^2 + \frac{r_X^2}{3}} \tag{7}$$

Equations 5−7 define the mathematical relationship between the radii and T, I, and C, where r_A, r_M, r_Y, and r_X correspond to the ionic radii of elements A, M, and X and the covalent radii of X, respectively. The derivations of eqs 5−7 can be found in the Supporting Information.

The ratio between eqs 3 and 4 was defined as the tolerance factor (t), as shown in eq 8. In the ideal case, the tolerance factor would be equal to 1. However, a deviation from 1 is expected due to the close packing assumption when relating the radii to the structural motifs (see the Supporting Information) and the cage-like nature of the $Yb_3Rh_4Sn_{13}$ structure type.

$$t = \frac{T + I}{C\sqrt{3}} \tag{8}$$

Herein, we present a Remeika tolerance factor for an intermetallic family. The Remeika tolerance factor requires only the ionic and covalent radii to determine if the $Yb_3Rh_4Sn_{13}$ or the $(Sn_{1-x}Er_x)Er_4Rh_6Sn_{18}$ structure type is plausible (details of the selected radii can be found in the Supporting Information). Such radii were selected because Remeika described the $Yb_3Rh_4Sn_{13}$ having covalent-ionic character.[35] Although the $Yb_3Rh_4Sn_{13}$ structure type is considered to be a cage-like structure, we have assumed a close packing arrangement to develop the geometrical descriptor with the assumption that the stable range will be offset from 1. The tolerance factor has been calculated for the possible combinations using lanthanides, Th, U, Y, Sc, group 8−10 transition metals, and tetrels (Si, Ge, and Sn), yielding 486 combinations. We later compiled all of the compounds adopting the $Yb_3Rh_4Sn_{13}$, $(Sn_{1-x}Er_x)Er_4Rh_6Sn_{18}$, and $(Sn_{1-x}Tb_x)Tb_4Rh_6Sn_{18}$ structure types and their respective hettotypes within the 486 combinations of elements. As a result, we have empirically determined the stability range of 0.68−0.83 for the $Yb_3Rh_4Sn_{13}$ structure type and >0.83 for the $(Sn_{1-x}Er_x)Er_4Rh_6Sn_{18}$ structure type and their corresponding hettotypes. Figure 6 highlights the stability region for $Yb_3Rh_4Sn_{13}$ and $(Sn_{1-x}Er_x)Er_4Rh_6Sn_{18}$ by plotting the calculated $T + I$ as a function of the calculated $\sqrt{3}C$ for all reported compounds. Most of the compounds are in their corresponding domain except for Yb and U analogues and the A−(Fe, Os)−Sn family. The disparity of the Yb and U analogues can be attributed to the fixed 3+ oxidation state for lanthanides and actinides used to calculate the corresponding tolerance factor values (see the Supporting Information). However, for instance, Yb can fluctuate between 3+ and 2+,

https://doi.org/10.1021/acs.chemmater.2c03711
Chem. Mater. 2023, 35, 2238−2247

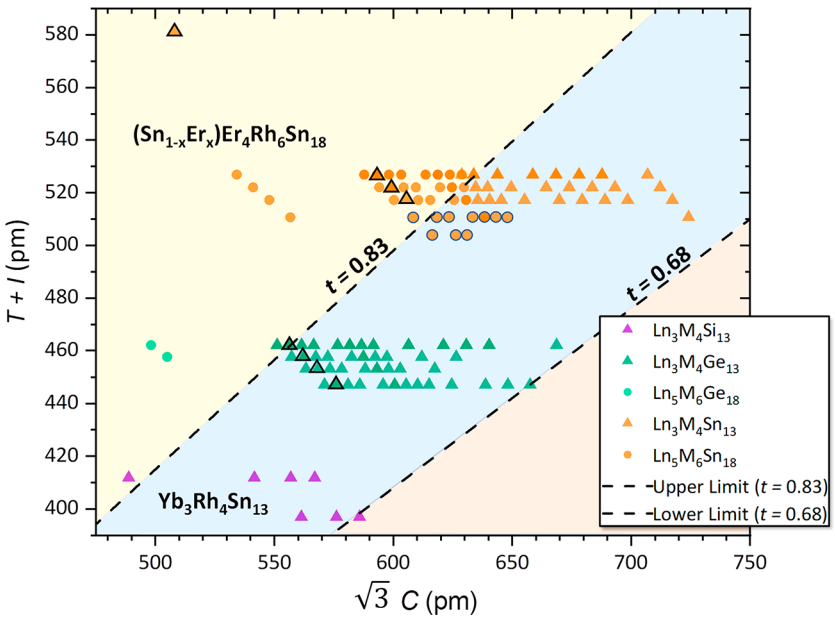

Figure 6. Graph of the calculated $T + I$ as a function of the calculated C for all of the reported $Yb_3Rh_4Sn_{13}$ (triangles) and $(Sn_{1-x}Er_x)Er_4Rh_6Sn_{18}$ (circles) structures and their respective hettotypes. The dotted lines correspond to t values of 0.83 and 0.68, which we empirically established as the $Yb_3Rh_4Sn_{13}$ structure type stability range, creating three domains. Moving from the top left to the bottom right, each domain corresponds to $(Sn_{1-x}Er_x)Er_4Rh_6Sn_{18}$, $Yb_3Rh_4Sn_{13}$, and unsynthesized, respectively. The color of the symbols corresponds to distinct X elements: purple for Si, green for Ge, and orange for Sn. The intensity of these colors is related to the overlap of data points. The delimited triangles correspond to Yb and U analogues, which are capable of valence fluctuation, while those in a concentered circle correspond to the A−(Fe, Os)−Sn family.

changing its ionic radii from 1.17 to ∼1.34 Å, which if taken into consideration would lower the tolerance factor value.

The formation of the $(Sn_{1-x}Er_x)Er_4Rh_6Sn_{18}$ structure type in the Fe−Sn and Os−Sn analogues is unexpected on the basis of their corresponding tolerance factor (see the Supporting Information). We first thought the discrepancy could arise from the ionic radius selected for Os and Fe; however, the germanide analogues are within their corresponding domain. The discrepancy is most likely due to electronic factors such as bonding character because the tolerance factor was built considering only geometrical constraints.

III.C. Discovery of a Predicted Phase: From Ce Intermetallics to $Yb_5Ru_6Sn_{18}$. The Remeika tolerance factor can be utilized to predict the presence of valence fluctuation in valence unstable lanthanides. As shown in eqs 7 and 8, the radius of the A element relates to the height of the cuboctahedron (C), which is inversely proportional to the tolerance factor. The tolerance factors for all of the compounds were calculated considering the ionic radius of element A in a 3+ oxidation state (see the Supporting Information). The radius of Ce^{3+} is 1.34 Å in a 12-coordinate environment, while that of Ce^{4+} is 1.14 Å.[54] Therefore, if we were to consider the valence fluctuation, the recalculated tolerance factor would increase and fall into what seems to be a more stable region. The Ce-based Remeika compounds that exemplify such observation are $Ce_3Os_4Ge_{13}$ (t = 0.68, 0.69 μ_B/Ce),[55] $Ce_3Ru_4Ge_{13}$ (t = 0.72, 1.06 μ_B/Ce),[56] $Ce_3Ir_4Ge_{13}$ (t = 0.72, 1.87 μ_B/Ce),[57] and $Ce_3Ru_4Sn_{13}$ (t = 0.77, 2.32 μ_B/Ce),[58] where the content of Ce^{4+} is inversely proportional to t. Interestingly, $Ce_3Co_4Sn_{13}$ (t = 0.75, 2.76 μ_B/Ce),[59] $Ce_3Rh_4Sn_{13}$ (t = 0.76, 2.55 μ_B/Ce),[60] and $Ce_3Ir_4Sn_{13}$ (t = 0.78, 2.56 μ_B/Ce)[61] deviate from the t−μ_B correlation. These compounds have been determined to undergo chiral phase transitions below 155 K,[59] 350 K,[60] and 600 K,[62] respectively. We believe the deviation from the effective magnetic moment trend is due to a different charge density distribution. Witas et al. presented a comparative study of $Ce_3M_4Sn_{13}$ (M = Co, Rh, and Ru) and highlighted the distinct charge density distribution between the group 9 transition metal analogues and Ru with the Sn atoms.[63] This points toward the Remeika tolerance factor being effective when relating to valence fluctuation but also highlights the importance of factors, such as covalency, in targeting the properties of interest.

With the goal of evaluating the predictability of the Remeika tolerance factor and its relationship with valence fluctuation, we have targeted the Yb−Ru−Sn phase (t = 0.89) because of the possible stabilization of the $Yb_3Rh_4Sn_{13}$ and $(Sn_{1-x}Er_x)$-$Er_4Rh_6Sn_{18}$ structure types. For valence fluctuating elements, such as Yb, it is less certain because each oxidation state would fall into different Remeika phase stability regions. For Yb−Ru−Sn phase, if Yb had mostly a Yb^{2+} character, the $Yb_3Rh_4Sn_{13}$ structure type would be expected, while for a higher Yb^{3+} character, the $(Sn_{1-x}Er_x)Er_4Rh_6Sn_{18}$ structure type would be expected. We have been able to synthesize $Yb_5Ru_6Sn_{18}$ and confirmed through magnetic susceptibility measurements mostly Yb^{3+} character, where the effective magnetic moment is 3.2 μ_B/Yb.

III.C.1. Synthesis and Structure Determination. Polycrystalline $Yb_5Ru_6Sn_{18}$ samples were first grown using the self-flux growth method.[64] Yb, Ru, and Sn were placed in a 5:6:18 ratio in a Canfield alumina crucible and sealed inside a fused silica tube under ∼$^1/_3$ atm of argon.[65] The resulting ampule was placed in a programmable furnace at 300 °C, heated to 850 °C at a rate of 100 °C/h, and dwelled for 48 h. The furnace was then cooled at a rate of 1 °C/h to 665 °C, at which point the ampule was rapidly removed, inverted, and centrifuged. The reaction product consisted of small polyhedral-shaped crystals of <0.1 mm.

https://doi.org/10.1021/acs.chemmater.2c03711
Chem. Mater. 2023, 35, 2238−2247

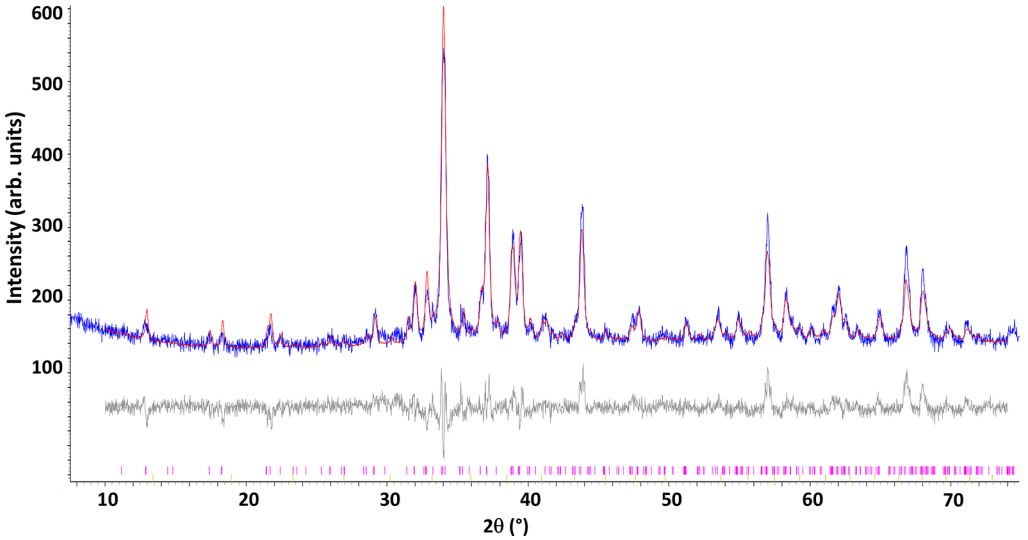

Figure 7. Powder X-ray diffraction pattern for $Yb_5Ru_6Sn_{18}$ [experimental (blue), refined (red), and difference (gray)] with the refined cell dimensions a = 13.72(1) Å and c = 27.44 (1) Å and space group $I4_1/acd$.

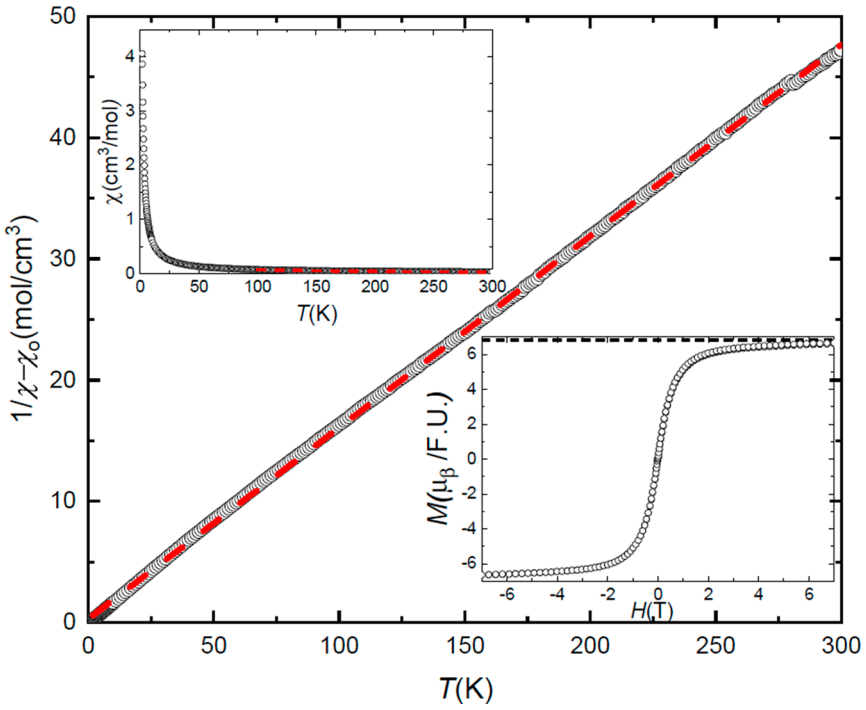

Figure 8. Modified Curie−Weiss fit (dotted red line) in the inverse magnetic susceptibility. The inset at the top left corresponds to the magnetic susceptibility as a function of temperature at 0.5 T. The inset at the bottom right corresponds to the magnetization as a function of applied field.

Powder X-ray diffraction data were collected using a Bruker D2 Phaser (Cu Kα radiation, λ = 1.54184 Å). The indexed powder diffraction pattern confirmed the formation of $Yb_5Ru_6Sn_{18}$ and small amounts of Sn. Figure 7 shows a fit of the data isostructural to tetragonal $(Sn_{1-x}Er_x)Er_4Rh_6Sn_{18}$.

Single-crystal X-ray diffraction data were obtained at room temperature using a Bruker D8 Quest Kappa single-crystal X-ray diffractometer with an IμS microfocus source (Mo Kα radiation, λ = 0.71073 Å) and a PHOTON II CPAD area detector. The raw data frames were processed using Bruker SAINT, and a multiscan absorption was corrected using SADABS.[66] The intrinsic phasing method and least-squares refinement were used in SHELXL to obtain preliminary starting models.[67] The reflections obtained through single-crystal X-ray diffraction were first indexed in the tetragonal crystal system with unit cell dimensions of a = 13.7142(9) Å and c = 27.436(4) Å. However, a full structure determination was not possible, and the presence of systematic unindexed reflections only observable in precession planes other than the $hk0$, $h0l$, and $0kl$ planes suggests the need for a supercell (see Figure S5). For further details regarding structure determination, see the Supporting Information.

III.C.2. Magnetic Susceptibility. The measurements of magnetic properties were performed on a collection of randomly oriented granular crystals using a Quantum Design Magnetic Property Measurement System (MPMS3). The

https://doi.org/10.1021/acs.chemmater.2c03711
Chem. Mater. 2023, 35, 2238−2247

temperature-dependent magnetic susceptibility $\chi = M/H$ was measured in an applied field (H) of 5000 Oe. A field-dependent magnetic isotherm was measured at 1.8 K for −70000 Oe < H < 70000 Oe. The magnetic susceptibility (χ) as a function of the temperature (T) was measured in a 0.5 T magnetic field, as shown in Figure 8. Paramagnetic behavior is observed between 1.8 and 300 K, with no evidence of magnetic ordering, where a modified Curie−Weiss law given by the expression $\chi(T) = \chi_0 + C/(T - \theta)$ is used to fit the data (Figure 8). This fit yields the parameters $\chi_0 = 0.011$ cm^3/mol, $C = 1.32$ cm^3/mol of Yb, and $\theta = -5.9$ K. The effective magnetic moment is determined to be 3.2 μ_B/Yb, which is lower than the expected values of 4.54 μ_B for Yb^{3+}. These results confirm a higher Yb^{3+} character, as was expected on the basis of the Remeika tolerance factor. A similar decrease in the effective magnetic moment has been observed for $Yb_5Pt_6In_{16}Bi_2$, which was reported with an effective magnetic moment of 3.72 μ_B/Yb.[68] Interestingly, the $Yb_5Pt_6In_{16}Bi_2$ crystal structure was not fully determined. Considering the superlattice reflections observed in our compound (see Figure S5), it seems inevitable to wonder if $Yb_5Pt_6In_{16}Bi_2$ also showed unindexed reflections at higher precession planes and if there is a possible connection between mixed valency and the appearance of the systematic weak reflections. This value is indicative of intermediate valence Yb f state behavior or Kondo lattice hybridization, similar to what is seen for β-$YbAlB_4$,[69,70] $Yb_2Ir_3Ge_5$,[71] and $YbNi_{2-x}Fe_xAl_8$ ($x = 0.91$).[72] The magnetization curve (Figure 8) shows a saturation value $M_s \approx 1.36$ μ_B/Yb, which also is reduced compared to the expected value of 4 μ_B for the full Yb^{3+} Hund's rule multiplet. In principle, a reduced low-temperature saturation moment might result from crystal electric field splitting of the Hund's rule multiplet, but we also infer that this value also relates to the reduced effective magnetic moment that is seen at higher temperatures.

IV. CONCLUSION AND FUTURE DIRECTION

Perovskites have been the target of numerous research groups due to their structural versatility, enabling high tunability. Such success could be attributed to the better understanding of the structural and electronic factors dictating stability. Goldschmidt's tolerance factor, charge balancing, and valence electron counting have been crucial for improving our understanding of perovskites and their variants. Such observations open the question of whether we can enhance the tunability of intermetallic compounds by better understanding the factors dictating stability.

Our group and others now seek to predict and synthesize new quantum materials by considering subunits[73] and geometric factors as a strategic first step. In the past decade, it has been demonstrated that several compounds adopting the Remeika phases show superconductivity and charge density waves. What is most intriguing is the properties typically not observed in 3D phases, such as charge density waves.[39,74] It would be strategic to have a model to predict phases to grow, inspire, and study the intrinsic properties of technological materials. Developing a tolerance factor for the Remeika phases, an overlooked intermetallic pseudoperovskite family of compounds, serves as an example for other intermetallic families and sets a foundation for further investigations of structure−property relationship. We foresee both electronic and structural factors as being essential precursors for not only predicting Remeika phases but also searching for materials at the verge of instability, which could lead to emergent states.

Finally, our results for $Yb_5Ru_6Sn_{18}$ invite further investigations into this material and its nearby chemical analogues. First, it will be useful to produce single-crystal specimens to assess the magnetic anisotropy and to confirm that the paramagnetic state unambiguously originates from a reduced Yb moment. Given its similarity to other intermediate valence and Kondo lattice compounds, it is also likely that this material will exhibit phenomena that originate from hybridization between the f and conduction electron states, e.g., heavy fermion or hybridization gap semiconductor ground state behavior. Heat capacity and electrical transport measurements will be useful for assessing this. Finally, there are very few Yb-based heavy fermion superconductors (e.g., $YbRh_2Si_2$ and β-$YbAlB_4$),[75] but the electronic and magnetic behavior of $Yb_5Ru_6Sn_{18}$ shares some similarities with theirs, opening the possibility for similar behavior under the right conditions.

Machine learning is promising in materials discovery, where statistical methods exploit the available data enhancing research.[76] The Remeika tolerance factor can provide a starting point for machine learning, increasing the number of available data points while testing the adaptability of the Remeika phases. While machine learning has been applied for perovskites for rational design,[77] prediction is only useful when synthesis and characterization are possible. Crystal growth is critical in determining and characterizing the intrinsic properties of materials.[9] The motivation has been discussed by several review articles and by no means extensively. However, the effective discovery of new phases with emergent properties, such as topological insulators, an anomalous quantum Hall effect, highly correlated materials, and unconventional superconductors, is highly inspiring. The horizon for new platforms for application awaits the community!

■ ASSOCIATED CONTENT

Supporting Information

The Supporting Information is available free of charge at https://pubs.acs.org/doi/10.1021/acs.chemmater.2c03711.

Additional mathematical equations and precession images (PDF)

Recompiled Remeika phases and tolerance calculator (XLSX)

■ AUTHOR INFORMATION

Corresponding Author

Julia Y. Chan − *Department of Chemistry and Biochemistry, Baylor University, Waco, Texas 76798, United States;* orcid.org/0000-0003-4434-2160; Email: Julia_Chan@baylor.edu

Authors

Alexis Dominguez Montero − *Department of Chemistry and Biochemistry, Baylor University, Waco, Texas 76798, United States*

Gregory T. McCandless − *Department of Chemistry and Biochemistry, Baylor University, Waco, Texas 76798, United States*

Olatunde Oladehin − *Department of Physics, Florida State University, Tallahassee, Florida 32306, United States; National High Magnetic Field Laboratory, Florida State University, Tallahassee, Florida 32310, United States*

Ryan E. Baumbach − *Department of Physics, Florida State University, Tallahassee, Florida 32306, United States; National High Magnetic Field Laboratory, Florida State University, Tallahassee, Florida 32310, United States*

Complete contact information is available at: https://pubs.acs.org/10.1021/acs.chemmater.2c03711

Notes

The authors declare no competing financial interest.

Biographies

Alexis Dominguez Montero received his B.S in Chemistry in 2019 from The University of Texas at Dallas. He is currently a Ph.D. candidate at Baylor University under the supervision of Dr. Julia Y. Chan studying new families of quantum materials exhibiting highly correlated systems.

Gregory McCandless is a research scientist in the Department of Chemistry and Biochemistry at Baylor University. He received his B.S. in Industrial Engineering and a Ph.D. in Chemistry from Louisiana State University in 2012. He has previously served as a crystallographer and enjoys structure determination of extended solids.

Olatunde Oladehin received his B.S. in Physics from the University of Ibadan, Nigeria. He obtained his first Master's in Applied Physical Science from Georgia Southern University and his second Master's in Physics from Florida States University. He is currently a Ph.D. candidate under the supervision of Dr. Ryan Baumbach, investigating the electronic states of topological metal.

Ryan Baumbach received his B.S. in Physics from the University of California, Santa Cruz, and a Ph.D. in Physics from the University of California, San Diego, in 2009. He was a postdoctoral researcher in the group of Professor M. Brian Maple at the University of California, San Diego, and a Director's funded postdoctoral researcher at the Los Alamos National Laboratory under the supervision of Dr. Eric Bauer. Since 2014, he has served as a Research Faculty at the National High Magnetic Field Laboratory at Florida State University and has held the honorary position of Research Professor in the Florida State University Department of Physics since 2017. His research team works at the interface of physics, chemistry, and materials science and is focused on crystal growth of highly correlated quantum materials.

Julia Chan received her B.S. in Chemistry from Baylor University and a Ph.D. in Chemistry from the University of California at Davis in 1998. She was a National Research Council Postdoctoral Fellow at the National Institute of Standards of Technology. In 2022, she was recruited to Baylor University where she is the Fenn Family Chair in Materials Science at the Department of Chemistry and Biochemistry. Her research team is at the interface of chemistry and physics and is focused on crystal growth of highly correlated quantum materials. She is an AAAS Fellow and currently serving as Deputy Editor for *Science Advances*.

■ ACKNOWLEDGMENTS

J.Y.C. and A.D.M. acknowledge NSF-DMR 2209804 and Welch AT-2056-20210327 for partial support of this work. The authors acknowledge DOE DE-SC0022068 for support as part of our synthesis strategy for growing a predicted phase. R.B. is supported by the National Science Foundation through NSF DMR-1904361. The National High Magnetic Field Laboratory is supported by the National Science Foundation through NSF DMR-1644779 and the State of Florida.

■ REFERENCES

(1) Kovnir, K. Predictive Synthesis. *Chem. Mater.* **2021**, *33* (13), 4835−4841.
(2) Klemm, W.; Busmann, E. Volumeninkremente und Radien einiger einfach negativ gelandener Ionen. *Z. Anorg. Allg. Chem.* **1963**, *319* (5−6), 297−311.
(3) Pauling, L. The Principles Determining the Structure of Complex Ionic Crystals. *J. Am. Chem. Soc.* **1929**, *51* (4), 1010−1026.
(4) The Nature of the Chemical Bond and the Structure of Molecules and Crystals. *Nature* **1941**, *148*, 3762677−677.
(5) Wade, K. Structural and Bonding Patterns in Cluster Chemistry. *Adv. Inorg. Chem. Radiochem.* **1976**, *18*, 1−66.
(6) Mingos, D. M. P. Polyhedral Skeletal Electron Pair Approach. A Generalised Principle for Condensed Polyhedra. *J. Chem. Soc., Chem. Commun.* **1983**, *12*, 706−708.
(7) Lin, Q.; Miller, G. J.; Corbett, J. D. Ordered $BaAl_4$-Type Variants in the $BaAu_xSn_{4-x}$ System: A Unified View on Their Phase Stabilities versus Valence Electron Counts. *lnorg. Chem.* **2014**, *53* (12), 5875−5877.
(8) Gladisch, F. C.; Steinberg, S. Revealing Tendencies in the Electronic Structures of Polar Intermetallic Compounds. *Crystals* **2018**, *8* (2), 80.
(9) Canfield, P. C. New Materials Physics. *Rep. Prog. Phys.* **2020**, *83* (1), No. 016501.
(10) Lin, Q.; Miller, G. J. Electron-Poor Polar Intermetallics: Complex Structures, Novel Clusters, and Intriguing Bonding with Pronounced Electron Delocalization. *Acc. Chem. Res.* **2018**, *51* (1), 49−58.
(11) Häussermann, U.; Amerioun, S.; Eriksson, L.; Lee, C.-S.; Miller, G. J. The s−p Bonded Representatives of the Prominent $BaAl_4$ Structure Type: A Case Study on Structural Stability of Polar Intermetallic Network Structures. *J. Am. Chem. Soc.* **2002**, *124* (16), 4371−4383.
(12) Xie, W.; Gustin, L.; Bian, G. 111-Type Semiconductor ReGaSi Follows 14e− Rules. *lnorg. Chem.* **2017**, *56* (9), 5165−5172.
(13) Luo, H.; Krizan, J. W.; Muechler, L.; Haldolaarachchige, N.; Klimczuk, T.; Xie, W.; Fuccillo, M. K.; Felser, C.; Cava, R. J. A Large Family of Filled Skutterudites Stabilized by Electron Count. *Nat. Commun.* **2015**, *6*, 6489.
(14) Yannello, V. J.; Fredrickson, D. C. Generality of the 18-n Rule: Intermetallic Structural Chemistry Explained through Isolobal Analogies to Transition Metal Complexes. *lnorg. Chem.* **2015**, *54* (23), 11385−11398.
(15) Goldschmidt, V. M. Die Gesetze der Krystallochemie. *Naturwissenschaften* **1926**, *14* (21), 477−485.
(16) Cai, L.; Arias, A. L.; Nino, J. C. The Tolerance Factors of the Pyrochlore Crystal Structure. *J. Mater. Chem.* **2011**, *21* (11), 3611−3618.
(17) Song, Z.; Liu, Q. Tolerance Factor and Phase Stability of the Normal Spinel Structure. *Cryst. Growth. Des.* **2020**, *20* (3), 2014−2018.
(18) Zhang, Y.; Shimada, T.; Kitamura, T.; Wang, J. Ferroelectricity in Ruddlesden−Popper Chalcogenide Perovskites for Photovoltaic Application: The Role of Tolerance Factor. *J. Phys. Chem. Lett.* **2017**, *8* (23), 5834−5839.
(19) Wang, F.; Zou, X.; Xu, M.; Wang, H.; Wang, H.; Guo, H.; Guo, J.; Wang, P.; Peng, M.; Wang, Z.; Wang, Y.; Miao, J.; Chen, F.; Wang, J.; Chen, X.; Pan, A.; Shan, C.; Liao, L.; Hu, W. Recent Progress on Electrical and Optical Manipulations of Perovskite Photodetectors. *Adv. Sci.* **2021**, *8* (14), 2100569.
(20) Long, G.; Sabatini, R.; Saidaminov, M. I.; Lakhwani, G.; Rasmita, A.; Liu, X.; Sargent, E. H.; Gao, W. Chiral-Perovskite Optoelectronics. *Nat. Rev. Mater.* **2020**, *5* (6), 423−439.
(21) Li, D.; Lee, K.; Wang, B. Y.; Osada, M.; Crossley, S.; Lee, H. R.; Cui, Y.; Hikita, Y.; Hwang, H. Y. Superconductivity in an Infinite-Layer Nickelate. *Nature* **2019**, *572* (7771), 624−627.
(22) Kobayashi, K. I.; Kimura, T.; Sawada, H.; Terakura, K.; Tokura, Y. Room-Temperature Magnetoresistance in an Oxide Material With

an Ordered Double-Perovskite Structure. *Nature* **1998**, *395* (6703), 677−680.
(23) DeMarco, M.; Blackstead, H. A.; Dow, J. D.; Wu, M. K.; Chen, D. Y.; Chien, F. Z.; Haka, M.; Toorongian, S.; Fridmann, J. Magnetic Phase Transition in Superconducting $Sr_2YRu_{0.95}Cu_{0.05}O_6$ Observed by The ^{99}Ru Mossbauer Effect. *Phys. Rev. B* **2000**, *62* (21), 14301−14303.
(24) Zhao, Y.; Daemen, L. L. Superionic Conductivity in Lithium-Rich Anti-Perovskites. *J. Am. Chem. Soc.* **2012**, *134* (36), 15042−15047.
(25) Zheng, J.; Perry, B.; Wu, Y. Antiperovskite Superionic Conductors: A Critical Review. *ACS Mater. Au* **2021**, *1* (2), 92−106.
(26) Xia, W.; Zhao, Y.; Zhao, F.; Adair, K.; Zhao, R.; Li, S.; Zou, R.; Zhao, Y.; Sun, X. Antiperovskite Electrolytes for Solid-State Batteries. *Chem. Rev.* **2022**, *122* (3), 3763−3819.
(27) Vasala, S.; Karppinen, M. $A_2B'B''O_6$ Perovskites: A Review. *Prog. Solid State Chem.* **2015**, *43* (1−2), 1−36.
(28) Maughan, A. E.; Ganose, A. M.; Almaker, M. A.; Scanlon, D. O.; Neilson, J. R. Tolerance Factor and Cooperative Tilting Effects in Vacancy-Ordered Double Perovskite Halides. *Chem. Mater.* **2018**, *30* (11), 3909−3919.
(29) Shi, C.; Yu, C.-H.; Zhang, W. Predicting and Screening Dielectric Transitions in a Series of Hybrid Organic-Inorganic Double Perovskites via an Extended Tolerance Factor Approach. *Angew. Chem.* **2016**, *55* (19), 5798−5802.
(30) Lyle Thomas, E.; Lee, H.-O.; Bankston, A. N.; MaQuilon, S.; Klavins, P.; Moldovan, M.; Young, D. P.; Fisk, Z.; Chan, J. Y. Crystal Growth, Transport, and Magnetic Properties of $Ln_3Co_4Sn_{13}$ (Ln = La, Ce) With a Perovskite-Like Structure. *J. Solid State Chem.* **2006**, *179* (6), 1642−1649.
(31) Rai, B. K.; Oswald, I. W. H.; Wang, J. K.; McCandless, G. T.; Chan, J. Y.; Morosan, E. Superconductivity in Single Crystals of $Lu_3T_4Ge_{13-x}$ (T = Co, Rh, Os) and $Y_3T_4Ge_{13-x}$ (T = Ir, Rh, Os). *Chem. Mater.* **2015**, *27* (7), 2488−2494.
(32) Rai, B. K.; Oswald, I. W. H.; Chan, J. Y.; Morosan, E. Intermediate Valence to Heavy Fermion Through a Quantum Phase Transition in $Yb_3(Rh_{1-x}T_x)_4Ge_{13}$ (T = Co, Ir) Single Crystals. *Phys. Rev. B* **2016**, *93* (3), No. 035101.
(33) Remeika, J. P.; Espinosa, G. P.; Cooper, A. S.; Barz, H.; Rowell, J. M.; McWhan, D. B.; Vandenberg, J. M.; Moncton, D. E.; Fisk, Z.; Woolf, L. D.; Hamaker, H. C.; Maple, M. B.; Shirane, G.; Thomlinson, W. A New Family of Ternary Intermetallic Superconducting/Magnetic Stannides. *Solid State Commun.* **1980**, *34* (12), 923−926.
(34) Espinosa, G. P. Crystal Growth and Crystal-Chemical Investigation of Systems Containing New Superconducting and/or Magnetic Ternary Stannides. *Mater. Res. Bull.* **1980**, *15* (6), 791−798.
(35) Hodeau, J. L.; Chenavas, J.; Marezio, M.; Remeika, J. P. The Crystal Structure of $SnYb_3Rh_4Sn_{12}$, a New Ternary Superconducting Stannide. *Solid State Commun.* **1980**, *36* (10), 839−845.
(36) Vandenberg, J. M. The Crystallography of New Ternary Compounds in the System Rare-Earth-Rhodium-Tin. *Mater. Res. Bull.* **1980**, *15* (6), 835−847.
(37) Hodeau, J. L.; Marezio, M.; Remeika, J. P. The Structure of $[Er(1)_{1-x}Sn(1)_x]Er(2)_4Rh_6Sn(2)_4Sn(3)_{12}Sn(4)_2$, a Ternary Reentrant Superconductor. *Acta. Cryst. B* **1984**, *B40*, 26−38.
(38) Oswald, I. W. H.; Rai, B. K.; McCandless, G. T.; Morosan, E.; Chan, J. Y. The Proof is in the Powder: Revealing Structural Peculiarities in the $Yb_3Rh_4Sn_{13}$ Structure Type. *CrystEngComm* **2017**, *19* (25), 3381−3391.
(39) Gumeniuk, R. Chapter 304 - Structural and Physical Properties of Remeika Phases. In *Handbook on the Physics and Chemistry of Rare Earths*; Bünzli, J.-C. G., Pecharsky, V. K., Eds.; Elsevier, 2018; Vol. *54*, pp 43−143.
(40) Fang, A. F.; Wang, X. B.; Zheng, P.; Wang, N. L. Unconventional Charge-Density Wave in $Sr_3Ir_4Sn_{13}$ Cubic Superconductor Revealed by Optical Spectroscopy Study. *Phys. Rev. B* **2014**, *90* (3), No. 035115.
(41) Welsch, J.; Ramakrishnan, S.; Eisele, C.; van Well, N.; Schönleber, A.; van Smaalen, S.; Matteppanavar, S.; Thamizhavel, A.; Tolkiehn, M.; Paulmann, C.; Ramakrishnan, S. Second-Order Charge-Density-Wave Transition in Single Crystals of $La_3Co_4Sn_{13}$. *Phys. Rev. Mater.* **2019**, *3* (12), 125003.
(42) Ban, W. J.; Wang, H. P.; Tseng, C. W.; Kuo, C. N.; Lue, C. S.; Wang, N. L. Optical Spectroscopy Study of Charge Density Wave Order in $Sr_3Rh_4Sn_{13}$ and $(Sr_{0.5}Ca_{0.5})_3Rh_4Sn_{13}$. *Sci. China: Phys. Mech. Astron.* **2017**, *60* (4), No. 047011.
(43) Wang, K.; Petrovic, C. $Ca_3Ir_4Sn_{13}$: A Weakly Correlated Nodeless Superconductor. *Phys. Rev. B* **2012**, *86* (2), No. 024522.
(44) Liu, X.; Zhang, W.; Lai, K. T.; Moriyama, K.; Tallon, J. L.; Yoshimura, K.; Goh, S. K. Peak in the Critical Current Density in $(Ca_xSr_{1-x})_3Rh_4Sn_{13}$ Tuned Towards the Structural Quantum Critical Point. *Phys. Rev. B* **2022**, *105* (21), 214524.
(45) Biswas, P. K.; Guguchia, Z.; Khasanov, R.; Chinotti, M.; Li, L.; Wang, K.; Petrovic, C.; Morenzoni, E. Strong Enhancement of s-wave Superconductivity Near a Quantum Critical Point of $Ca_3Ir_4Sn_{13}$. *Phys. Rev. B* **2015**, *92* (19), 195122.
(46) Iwasa, K.; Suyama, K.; Ohira-Kawamura, S.; Nakajima, K.; Raymond, S.; Steffens, P.; Yamada, A.; Matsuda, T. D.; Aoki, Y.; Kawasaki, I.; Fujimori, S.-i.; Yamagami, H.; Yokoyama, M. Weyl-Kondo Semimetal Behavior in the Chiral Structure Phase of $Ce_3Rh_4Sn_{13}$. *Phys. Rev. Mater.* **2023**, *7* (1), No. 014201.
(47) Bordet, P.; Miraglia, S.; Hodeau, J. L.; Marezio, M. Competition Between Magnetism and Superconductivity in Erbium Rhodium Stannide. *J. Solid State Chem.* **1999**, *147* (1), 399−409.
(48) Espinosa, G. P.; Cooper, A. S.; Barz, H.; Remeika, J. P. Crystal Chemistry, Growth and Reentrant Behavior of Additional Superconducting/Magnetic Stannides. *Mater. Res. Bull.* **1980**, *15* (11), 1635−1641.
(49) Bhattacharyya, A.; Adroja, D.; Kase, N.; Hillier, A.; Akimitsu, J.; Strydom, A. Unconventional Superconductivity in $Y_5Rh_6Sn_{18}$ Probed by Muon Spin Relaxation. *Sci. Rep.* **2015**, *5* (1), 12926.
(50) Bhattacharyya, A.; Adroja, D. T.; Kase, N.; Hillier, A. D.; Strydom, A. M.; Akimitsu, J. Unconventional Superconductivity in the Cage-Type Compound $Sc_5Rh_6Sn_{18}$. *Phys. Rev. B* **2018**, *98* (2), No. 024511.
(51) Bhattacharyya, A.; Adroja, D. T.; Quintanilla, J.; Hillier, A. D.; Kase, N.; Strydom, A. M.; Akimitsu, J. Broken Time-Reversal Symmetry Probed by Muon Spin Relaxation in the Caged Type Superconductor $Lu_5Rh_6Sn_{18}$. *Phys. Rev. B* **2015**, *91* (6), No. 060503.
(52) Wang, C.-W.; Karna, S. K.; Yano, S.-i.; Lee, C.-H.; Avdeev, M.; Lue, C. S.; Kuo, C. N. Magnetic Properties and Noncollinear Spin Structure of the Tin-Rich Stannide $Ho_5Co_6Sn_{18}$. *Phys. Rev. B* **2022**, *105* (10), 104429.
(53) Krenkel, E. H.; Tanatar, M. A.; Kończykowski, M.; Grasset, R.; Timmons, E. I.; Ghimire, S.; Joshi, K. R.; Lee, Y.; Ke, L.; Chen, S.; Petrovic, C.; Orth, P. P.; Scheurer, M. S.; Prozorov, R. Possible Unconventional Pairing in $(Ca, Sr)_3(Ir,Rh)_4Sn_{13}$ Superconductors Revealed by Controlling Disorder. *Phys. Rev. B* **2022**, *105* (9), No. 094521.
(54) Shannon, R. D. Revised Effective Ionic Radii and Systematic Studies of Interatomic Distances in Halides and Chalcogenides. *Acta Crystallogr., Sect. A* **1976**, *32* (5), 751−767.
(55) Prakash, O.; Thamizhavel, A.; Ramakrishnan, S. Ferromagnetic Ordering of Minority Ce^{3+} Spins in a Quasi-Skutterudite $Ce_3Os_4Ge_{13}$ Single Crystal. *Phys. Rev. B* **2016**, *93* (6), No. 064427.
(56) Ghosh, K.; Ramakrishnan, S.; Dhar, S. K.; Malik, S. K.; Chandra, G.; Pecharsky, V. K.; Gschneidner, K. A.; Hu, Z.; Yelon, W. B. Crystal Structures and Low-Temperature Behaviors of the Heavy-Fermion Compounds $CeRuGe_3$ and $Ce_3Ru_4Ge_{13}$ Containing Both Trivalent and Tetravalent Cerium. *Phys. Rev. B* **1995**, *52* (10), 7267−7277.
(57) Hallas, A. M.; Huang, C. L.; Rai, B. K.; Weiland, A.; McCandless, G. T.; Chan, J. Y.; Beare, J.; Luke, G. M.; Morosan, E. Complex Transport and Magnetism in Inhomogeneous Mixed Valence $Ce_3Ir_4Ge_{13}$. *Phys. Rev. Mater.* **2019**, *3* (11), 114407.

https://doi.org/10.1021/acs.chemmater.2c03711
Chem. Mater. 2023, 35, 2238−2247

(58) Lee, J.; Mun, E. Physical Properties of $Ce_{3+x}Ru_4Sn_{13-x}$ Single Crystals. *Phys. Rev. Mater.* **2022**, *6* (4), No. 043401.
(59) Otomo, Y.; Iwasa, K.; Suyama, K.; Tomiyasu, K.; Sagayama, H.; Sagayama, R.; Nakao, H.; Kumai, R.; Murakami, Y. Chiral Crystal-Structure Transformation of $R_3Co_4Sn_{13}$ (R = La and Ce). *Phys. Rev. B* **2016**, *94* (7), No. 075109.
(60) Suyama, K.; Iwasa, K.; Otomo, Y.; Tomiyasu, K.; Sagayama, H.; Sagayama, R.; Nakao, H.; Kumai, R.; Kitajima, Y.; Damay, F.; Mignot, J.-M.; Yamada, A.; Matsuda, T. D.; Aoki, Y. Chiral-Crystal-Structure Transformations and Magnetic States of $R_3Rh_4Sn_{13}$ (R = La and Ce). *Phys. Rev. B* **2018**, *97* (23), 235138.
(61) Nagoshi, C.; Sugawara, H.; Aoki, Y.; Sakai, S.; Kohgi, M.; Sato, H.; Onimaru, T.; Sakakibara, T. Anomalous Phase Transitions in the Heavy Fermion Compound $Ce_3Ir_4Sn_{13}$. *Physica B Condens. Matter* **2005**, *359*−*361*, 248−250.
(62) Iwasa, K.; Nakazato, S.; Hashimoto, D.; Shiozawa, M.; Kuwahara, K.; Sagayama, H.; Ohira-Kawamura, S.; Murai, N.; Adroja, D. T.; Strydom, A. M. Magnetic Excitations in Chiral-Structure Phase of $Ce_3Ir_4Sn_{13}$. *J. Phys. Soc. Jpn.* **2021**, *90* (12), 124701.
(63) Ślebarski, A.; Goraus, J.; Witas, P. Electrical Resistivity of The Heavy-Fermion-Filled Cage Compound $Ce_3M_4Sn_{13}$(M = Co,Rh,Ru) Under High Pressure. *Phys. Rev. B* **2015**, *92* (15), 155136.
(64) Canfield, P. C.; Fisk, Z. Growth of Single Crystals From Metallic Fluxes. *Philos. Mag. B* **1992**, *65* (6), 1117−1123.
(65) Canfield, P. C.; Kong, T.; Kaluarachchi, U. S.; Jo, N. H. Use of Frit-Disc Crucibles for Routine and Exploratory Solution Growth of Single Crystalline Samples. *Philos. Mag.* **2016**, *96* (1), 84−92.
(66) Krause, L.; Herbst-Irmer, R.; Sheldrick, G. M.; Stalke, D. Comparison of Silver and Molybdenum Microfocus X-Ray Sources for Single-Crystal Structure Determination. *J. Appl. Crystallogr.* **2015**, *48* (1), 3−10.
(67) Sheldrick, G. Crystal Structure Refinement with SHELXL. *Acta Crystallogr., Sect. C* **2015**, *71* (1), 3−8.
(68) Moshopoulou, E. G.; Hundley, M. F.; Movshovich, R.; Thompson, J. D.; Sarrao, J. L.; Fisk, Z.; Felder, E.; Chernikov, M.; Pushin, D.; Ott, H. R. Structure and Physical Properties of the Quaternary Remeika-Phase Compound $Yb_5Pt_6In_{16}Bi_2$. *Phys. Rev. B* **1999**, *60* (6), 4096−4100.
(69) Matsumoto, Y.; Kuga, K.; Karaki, Y.; Shimura, Y.; Sakakibara, T.; Tokunaga, M.; Kindo, K.; Nakatsuji, S. Field Evolution of Quantum Critical and Heavy Fermi-Liquid Components in the Magnetization of the Mixed Valence Compound β-$YbAlB_4$. *J. Phys. Soc. Jpn.* **2015**, *84* (2), No. 024710.
(70) Nakatsuji, S.; Kuga, K.; Machida, Y.; Tayama, T.; Sakakibara, T.; Karaki, Y.; Ishimoto, H.; Yonezawa, S.; Maeno, Y.; Pearson, E.; Lonzarich, G. G.; Balicas, L.; Lee, H.; Fisk, Z. Superconductivity and Quantum Criticality in the Heavy-Fermion System β-$YbAlB_4$. *Nat. Phys.* **2008**, *4* (8), 603−607.
(71) Singh, Y.; Ramakrishnan, S. Physical Properties of the Kondo-Lattice Compound $Yb_2Ir_3Ge_5$. *Phys. Rev. B* **2003**, *68* (5), No. 054419.
(72) Wu, X.; Francisco, M.; Rak, Z.; Bakas, T.; Mahanti, S. D.; Kanatzidis, M. G. Synthesis, Magnetism and Electronic Structure of $YbNi_{2-x}Fe_xAl_8$ (x = 0.91) Isolated from Al Flux. *J. Solid State Chem.* **2008**, *181* (12), 3269−3277.
(73) Lai, Y.; Chan, J. Y.; Baumbach, R. E. Electronic Landscape of the *f*-Electron Intermetallics with the $ThCr_2Si_2$ Structure. *Sci. Adv.* **2022**, *8* (32), eabp8264.
(74) Carneiro, F. B.; Veiga, L. S. I.; Mardegan, J. R. L.; Khan, R.; Macchiutti, C.; López, A.; Bittar, E. M. Unveiling Charge Density Wave Quantum Phase Transitions by X-ray Diffraction. *Phys. Rev. B* **2020**, *101* (19), 195135.
(75) Schuberth, E.; Tippmann, M.; Steinke, L.; Lausberg, S.; Steppke, A.; Brando, M.; Krellner, C.; Geibel, C.; Yu, R.; Si, Q.; Steglich, F. Emergence of Superconductivity in the Canonical Heavy-Electron Metal $YbRh_2Si_2$. *Science* **2016**, *351* (6272), 485−488.
(76) Schmidt, J.; Marques, M. R. G.; Botti, S.; Marques, M. A. L. Recent Advances and Applications of Machine Learning in Solid-State Materials Science. *npj Comput. Mater.* **2019**, *5* (1), 83.
(77) Tao, Q.; Xu, P.; Li, M.; Lu, W. Machine Learning for Perovskite Materials Design and Discovery. *npj Comput. Mater.* **2021**, *7* (1), 23.

https://doi.org/10.1021/acs.chemmater.2c03711
Chem. Mater. 2023, 35, 2238−2247